

# SphereSR: 360° Image Super-Resolution with Arbitrary Projection via Continuous Spherical Image Representation

Youngho Yoon, Inchul Chung, Lin Wang, and Kuk-Jin Yoon  
Visual Intelligence Lab., KAIST, Korea

{dudgh1732, inchul1221, wanglin, kjyoon}@kaist.ac.kr

## Abstract

The 360° imaging has recently gained great attention; however, its angular resolution is relatively lower than that of a narrow field-of-view (FOV) perspective image as it is captured by using fisheye lenses with the same sensor size. Therefore, it is beneficial to super-resolve a 360° image. Some attempts have been made but mostly considered the equirectangular projection (ERP) as one of the way for 360° image representation despite of latitude-dependent distortions. In that case, as the output high-resolution (HR) image is always in the same ERP format as the low-resolution (LR) input, another information loss may occur when transforming the HR image to other projection types. In this paper, we propose SphereSR, a novel framework to generate a continuous spherical image representation from an LR 360° image, aiming at predicting the RGB values at given spherical coordinates for super-resolution with an arbitrary 360° image projection. Specifically, we first propose a feature extraction module that represents the spherical data based on icosahedron and efficiently extracts features on the spherical surface. We then propose a spherical local implicit image function (SLIIF) to predict RGB values at the spherical coordinates. As such, SphereSR flexibly reconstructs an HR image under an arbitrary projection type. Experiments on various benchmark datasets show that our method significantly surpasses existing methods.

## 1. Introduction

The 360° imaging has recently gained great attention in many fields including AR/VR. In general, raw 360° images are transformed into 2D planar representations preserving the omnidirectional information, e.g., equirectangular projection (ERP) [16] and cube map projection (CP) [16] to be compatible with the imaging pipelines. The omnidirectional images (ODIs)<sup>1</sup> are sometimes projected back onto a sphere or transformed with different types of projection and rendered for display in some applications.

<sup>1</sup>Throughout the paper, we use omnidirectional images and 360° images interchangeably.

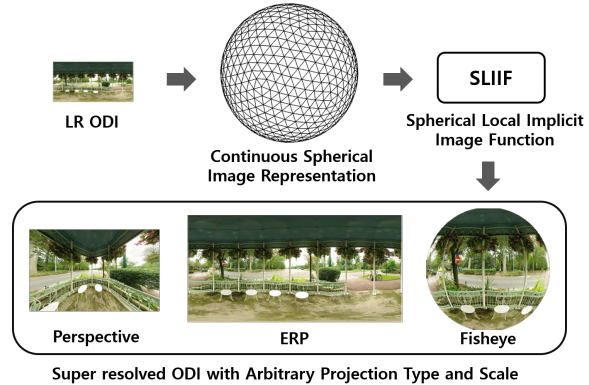


Figure 1. Learning continuous spherical image representation. SphereSR leverages SLIIF to predict the RGB values at given spherical coordinates for SR with arbitrary image projection.

However, the angular resolution of a 360° image tends to be lower than that of a narrow field-of-view (FOV) perspective image as it is captured using fisheye lenses with the same sensor size. Moreover, the 360° image quality can be degraded during the transformation between different image projection types. Therefore, it is imperative to super-resolve the low-resolution (LR) 360° image by considering various projections to provide a high-level visual quality in diverse conditions. Early studies have attempted to reconstruct high-resolution (HR) ODIs by interpolating the missing data between the LR image pixels [3, 5, 26].

Recently, deep learning (DL) has brought a significant performance boost for the 2D single image super-resolution (SISR) [18, 38, 45]. These methods mostly explore super-resolving the 2D LR image using high-capacity convolutional neural networks (CNNs), via e.g., residual connections [22], and learning algorithms including generative adversarial networks (GANs) [19, 41, 42]. However, directly using these methods for 360° images represented in 2D planar representations is less applicable as the pixel density and texture complexity vary across different positions in 2D planar representations of 360° images, as pointed in [10].

Consequently, some attempts have been made to address the SR problems for 360° imaging [10, 29, 37, 47]. In par-

ticular, 360-SS [29] proposes a GAN-based framework using the Pix2Pix pipeline [14]; however, it focuses only on the ERP format and does not fully consider the properties of 360° images. LAU-Net [10] introduces a method to identify distortions of an ODI on the latitude and upsample the ODI pixels on the segmented patches. However, it leads to considerable disconnections along the patches. In a nutshell, existing methods for ODI SR ignore the projection process of 360° images in real applications and only take the ERP image as the LR input and produce the HR ERP output. Indeed, the 360° image can be flexibly converted into various projection types as, in real applications, user specifies the projection type, direction, and FOV. Thus, it is vital to address the ERP distortions problems and strive to super-resolve an ODI image to an HR image with *an arbitrary projection type* rather than a fixed type.

In this paper, as shown in Fig. 1, we propose a novel framework, called SphereSR, aiming at super-resolving an LR 360° image to an HR image *with an arbitrary projection type via continuous spherical image representation*. First, we propose a feature extraction module that represents the spherical data based on icosahedron and efficiently extracts features on the spherical surface composed of uniform faces (Sec. 3.1). As such, we solve the ERP image distortion problem and the pixel density difference according to the latitude. Second, we propose a spherical local implicit image function (SLIIF) that can predict RGB values at arbitrary coordinates of a sphere feature map, inspired by LIIF [7] (Sec. 3.2). SLIIF works on *triangular face*, buttressed by the position embedding based on the normal plane polar coordinates to obtain relative coordinates on a sphere. Therefore, our method tackles pixel-misalignment issue when being projected to another ODI projection. As a result, SphereSR can predict RGB values for any SR scale parameters. Additionally, to train SphereSR, we introduce a feature loss that measures the similarity between two projection types, leading to considerable performance enhancement (Sec. 3.3). Extensive experiments on various benchmark datasets show that our method significantly surpasses existing methods.

In summary, the contributions of our paper are four-fold. (I) We propose a novel framework, called SphereSR, aiming at super-resolving an LR 360° image to an HR image with an arbitrary projection type. (II) We propose a feature extraction module that represents the spherical data based on icosahedron and extracts features on spherical surface. (III) We propose SLIIF that predicts RGB values from the spherical coordinates. (IV) Our method achieves the significantly better performance in the extensive experiments.

## 2. Related Works

**Omnidirectional Image SR and Enhancement.** Early ODI SR methods [2, 4, 6, 15, 27] focused on assembling

and optimizing multiple LR ODIs on spherical or hyperbolic surface. On the other hand, as the distortion in ODI is caused due to the projection of original spherical image to the 2D planar image plane, recent research focused on tackling and solving distortion in ODI using 2D convolution to achieve qualitative result in observation space, *i.e.* spherical surface. Su *et al.* [37] and Zhou *et al.* [47] proposed evaluation methods for ODI weighted with the projected area on the spherical surface. [31] and [28] adapted existing SISR models to ERP SR by fine-tuning or by adding a distortion map as an input to tackle different distortions. [29] leveraged GAN to super-resolve an ODI by applying WS-SSIM [47]. [46] also proposed the GAN-based framework employing multi-frequency structures to enhance the panoramic image quality up to the high-end camera quality. [23] focused on the 360° image SR utilizing single-frame and multi-frame joint learning and a loss function weighted differently along the latitude. [10] considered varying pixel density and texture complexity along latitude by proposing network allowing distinct up-scaling factors along the latitude bands. *Unlike the aforementioned methods, we propose to predict the RGB values at the given spherical coordinates of an HR image with respect to an arbitrary project type from an LR 360° image.*

**2D SISR with an Arbitrary Scale.** Research on SISR with an arbitrary scale has been actively conducted. [22] first proposed a method that enables multiple scale factors over one network. MetaSR [13] achieves SR with the non-integer scale factors. However, both methods are limited to SR with the symmetric scales. Later on, [40] proposed a framework that enables asymmetric scale factors along horizontal and vertical axes. Moreover, SRWarp [35] generalizes SR toward an arbitrary image transformation. Although these methods are effective for 2D SISR with an arbitrary scale factor, they fail to be directly applied to 360° image SR due to the difference between xy-coordinate (2D) and spherical coordinates in ODI domains. *We overcome the challenge by proposing SphereSR that leverages SLIIF to predict RGB values for the arbitrary spherical coordinates.*

**Continuous Image Representation.** Research on implicit neural representation (INR) has been conducted to express 3D spaces, *e.g.*, 3D shape construction and novel view synthesis as continuous ways [24, 25, 33]. Since then, continuous image representation has been explored on the (x,y) coordinate. [1, 34] used the networks to predict the RGB value of each pixel from the latent vector on (x,y) coordinate without a spatial convolution for 2D image generation. LIIF [7] proposes to bridge between discrete and continuous representation for images on the (x,y) coordinate. *We propose SLIIF that makes continuous image representation on the unit sphere possible.*

**CNNs for Spherical Images.** [8] proposed a CNN-based method on the sphere with structural characteristics called

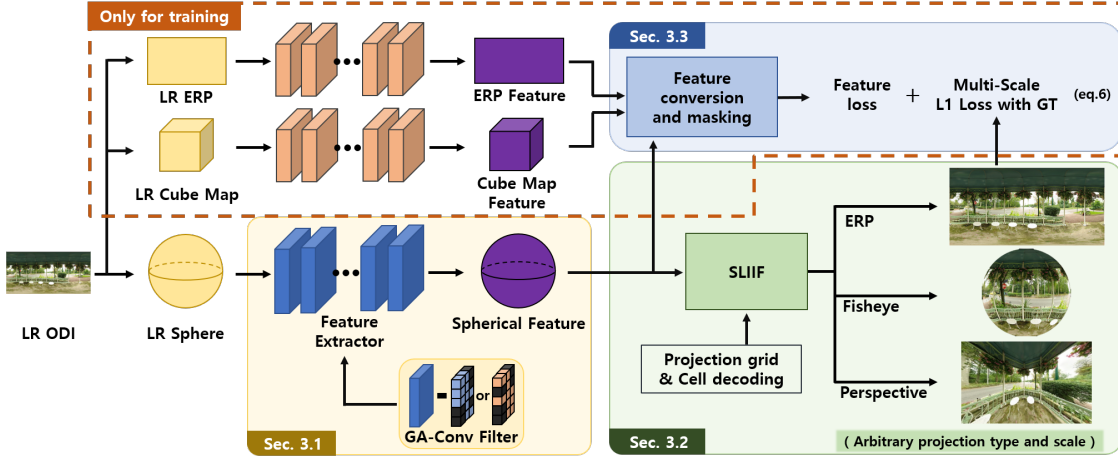


Figure 2. Overall framework of the proposed SphereSR.

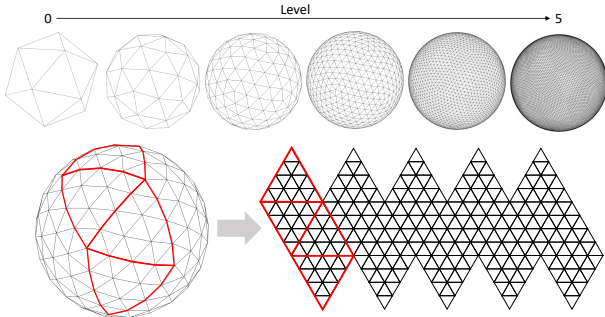


Figure 3. Subdivision process of icosahedron. We define a pixel as a face of subdivided icosahedron.

rotational equivariance. However, it requires Fourier transform for each step. [9] developed a CNN filter in light of spatial location on the sphere to solve the distortion problem of the ERP images. [36] proposed a kernel transformer network that converts the pre-trained kernels on the perspective images into ODIs. SpherePHD [20] proposed a convolution kernel applicable to triangular pixels defined on the faces of the icosahedron. [44] performed convolution using a hexagonal filter applicable to the vertices of icosahedron. In this work, we focus on ODI SR and propose SphereSR that applies convolution to the spherical structure created through the subdivision of the icosahedron.

### 3. Method

**Overview.** As shown in Fig. 2, we propose a novel framework, SphereSR, that aims at obtaining a continuous spherical image representation from a given icosahedron input. First, we introduce a feature extraction method for spherical images that efficiently extracts features from an image on the icosahedron (Sec. 3.1). Second, we propose the Spherical Local Implicit Image Function (SLIIF) that can predict RGB values through the extracted features in order to flexibly reconstruct an HR image with arbitrary projection type (Sec. 3.2). Lastly, We propose a feature loss to obtain

support from features of other projection types by utilizing the advantage of SLIIF that can be converted to arbitrary projection type (Sec. 3.3).

#### 3.1. Feature Extraction for Spherical Images

Feature extraction is crucial yet challenging for spherical image SR as we focus on very large scale factors, *e.g.*,  $\times 16$ . In this situation, *it is imperative to tackle the memory overload issue while ensuring high SR performance*. For that reason, the proposed SphereSR represents the spherical data based on icosahedron and efficiently extracts features on the spherical surface composed of uniform faces. This is achieved by a new data structure on icosahedron and weight sharing between kernels of different directions.

**Data structure.** Inspired by the convolution of icosahedron data in SpherePHD, we propose a new spherical data structure. To implement the convolution operation, SpherePHD [20] uses the subdivision process of icosahedron described in Fig. 3 and creates a call-table containing the indices of  $N$  neighboring pixels for each pixel and then uses it to stack every neighboring pixel. After that, convolution is performed with the kernel of size  $[N + 1, 1]$ . However, this implementation is not memory-efficient as it requires additional  $N$  channels for stacking the neighboring pixels for every convolution operation. To solve this problem, we propose a new data structure that convolution operation can be directly applied without stacking the neighbors in a call-table. As shown in the left side of Fig. 4, we rearrange the original data in the direction of the arrow while transforming the triangular pixels to rectangular pixels such that conventional 2D convolution can be applied. Here, an upward kernel (red kernel) for the upward( $\triangle$ ) aligned pixel is arranged in the odd-numbered rows, and a downward kernel (blue kernel) for the downward( $\nabla$ ) aligned pixel is arranged in the even-numbered rows. (More details are in the supplementary.)

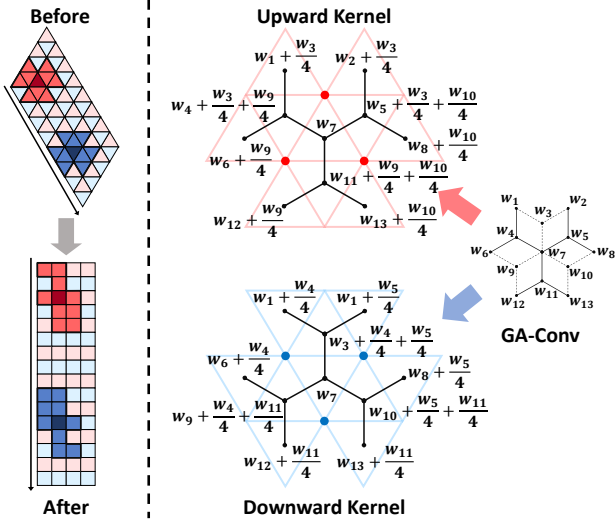


Figure 4. New kernel weight sharing. Left: proposed new data structure, Right: our kernel weight sharing scheme

**Kernel Weight Sharing.** While the memory overload issue can be resolved by the proposed data structure, it is still necessary to ensure high SR performance. SpherePHD [20] rotates the upward or downward kernel by  $180^\circ$  to obtain the same kernel shape. Therefore, it is possible to share weights of the up/downward kernels whose directions and shapes are symmetric to each other. However, as the direction of the kernel weight changes for adjacent pixels, high performance cannot be achieved if the characteristics of the texture according to the direction need to be identified.

To solve this problem, we introduce a kernel weight sharing scheme that can geometrically align up/downward directional kernels *without rotation*. As shown in the right side of Fig. 4, pixel(face) combinations of two kernels, where up/downward kernels are applied, are shaped differently depending on the direction of a center pixel. However, if three vertices of the center pixel (denoted as **red** and **blue** dots in the right side of Fig. 4) are included in the pixel combination as imaginary pixels, the shapes of two different up/downward pixel combinations can be made to be geometrically identical. To this end, rather than averaging and creating imaginary pixels, we distribute the kernel weight to near pixels. For the upward kernel, image pixel weight  $w_3, w_9, w_{10}$  are distributed to the nearest 4 pixels except the center pixel. For downward kernel weight,  $w_4, w_5, w_{11}$  are distributed in the same way. The detail can be seen in the right side of Fig. 4. In this way, the feature extraction module can be applied to any pixel without rotation.

### 3.2. Spherical Local Implicit Image Function (SLIIF)

**Overall Process of SLIIF.** With the data efficiently represented, we now describe how to super-resolve the ODIs efficiently with an arbitrary scale. Our main idea is to predict an RGB value for an arbitrary coordinate on the unit sphere

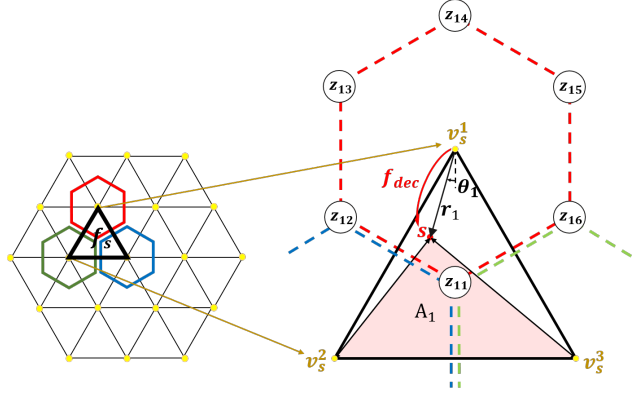


Figure 5. Spherical local implicit image function.

$S^2$  using the feature map extracted by using GA-Conv described in Sec. 3.1. Inspired by LIIF [7], we propose SLIIF that learns an implicit image function on  $S^2$  using icosahedral faces. SLIIF takes a spherical coordinate of the point on the unit sphere and its neighboring feature vectors as inputs and predicts the RGB value. It can be formulated as:

$$I(s) = f_{dec}(z, s), s \in S^2 \quad (1)$$

where  $f_{dec}$  is a decoding function shared with all icosahedral faces,  $s$  is the point on the unit sphere  $S^2$ ,  $z$  represents a feature vector formed by concatenating neighboring feature vectors of  $s$ , and  $I(s)$  is the predicted RGB value of  $s$ .

For the pixel in the image that can be formed by any arbitrary projection from the unit sphere, there is a corresponding point  $s$  on the unit sphere  $S^2$ .<sup>2</sup> The face containing  $s$  is denoted as  $f_s$  and three vertices surrounding  $f_s$  are denoted as  $v_s^1, v_s^2, v_s^3$  (see Fig. 5). The RGB values of  $s$  w.r.t. the coordinate system of three vertices are first calculated and then ensembled based on the triangular areas  $A_1, A_2, A_3$  to get the final RGB value of point  $s$ . The RGB value of  $s$  w.r.t. each vertex  $v_s^j$  is calculated with features of 6 faces containing the vertex and relative polar coordinate. The features of the six faces are concatenated clock-wise starting from  $f_s$  to preserve geometrical consistency. Here, we denote the concatenated features as  $z_j$  and the polar coordinate of  $s$  with respect of  $v_s^j$  as  $(r_j, \theta_j)$ . To better utilize the positional information,  $(r_j, \theta_j)$  are encoded with  $\gamma(p) = (\sin(2^0 \pi p), \cos(2^0 \pi p), \dots, \sin(2^{L-1} \pi p), \cos(2^{L-1} \pi p))$  to extend the dimension of a relative coordinate introduced in [25, 39]. As such, we can predict the RGB value of point  $(\theta, \phi) \in S^2$ , which can be formulated as:

$$I(\theta, \phi) = \sum_{j=1}^3 \frac{A_j}{A} \cdot f_{dec}(z_j, [\gamma(r_j), \gamma(\theta_j)]) \quad (2)$$

When the pixel in the image corresponds to the vertex on  $S^2$ , we can still follow the aforementioned procedure be-

<sup>2</sup>The coordinate of  $s$  is computed by using the center point of a pixel.

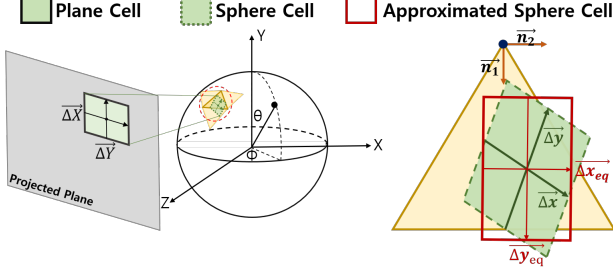


Figure 6. Sphere-oriented Cell Decoding.

cause any choice of neighboring vertices results in the same RGB value due to the triangle area-based weighting.

**Sphere-oriented Cell Decoding.** Through SLIIF, we can predict the RGB value for any point on  $S^2$ . That is, we can generate the desired HR image for any projection type by predicting the RGB value of each pixel. However, SLIIF provides the RGB value only for the center of the pixel and discards the information within the pixel area except for the center value. To handle this, LIIF [7] defines the cell decoding value as the width and height of the query pixel of interest. Nonetheless, this definition cannot be directly applied to sphere as the corresponding region on the sphere is not in a rectangular shape, and the direction of the reference vertex, where the RGB value is first calculated, continually changes. To handle this, we propose sphere-oriented cell decoding, a method considering the relation between the pixel region on the projected output and the corresponding region on  $S^2$ . By adding the cell decoding value as the input to SLIIF, we can fully utilize information within the pixel area. As shown in Fig. 6, we aim at obtaining the RGB value of the rectangular pixel on the projected plane. We call this rectangular pixel a plane cell, which can be expressed using two vectors  $\overrightarrow{\Delta X}$ ,  $\overrightarrow{\Delta Y}$ . The sphere cell, the corresponding area of the plane cell on the sphere, is located in the face where the corresponding point of pixel center is located on the sphere. The sphere cell can be also expressed using two vectors  $\overrightarrow{\Delta x}$ ,  $\overrightarrow{\Delta y}$ . The relation between  $\overrightarrow{\Delta X}$ ,  $\overrightarrow{\Delta Y}$  and  $\overrightarrow{\Delta x}$ ,  $\overrightarrow{\Delta y}$  depends on the projection type and location of the pixel center (refer to the supplementary for details).

For the geometrical consistency of the orders of the concatenated features, relative coordinate of  $s$ , and cell decoding value among pixels, we need to define new axis vectors,  $\overrightarrow{n_1}$  and  $\overrightarrow{n_2}$ , invariant to face orientation. The unit vector  $\overrightarrow{n_1}$  is defined as a vector between the reference vertex and the face center, and the unit vector  $\overrightarrow{n_2}$  is defined by 90 degree counter-clockwise rotation of  $\overrightarrow{n_1}$ . To get the height and width based on this coordinate system, we approximate the parallelogram sphere cell to the axis-aligned rectangle. The approximated sphere cell is defined as a rectangle which can be expressed using two vectors  $\overrightarrow{\Delta x_{eq}}$ ,  $\overrightarrow{\Delta y_{eq}}$  that has the same area as the parallelogram sphere cell and the largest intersection area with the parallelogram sphere cell. Based

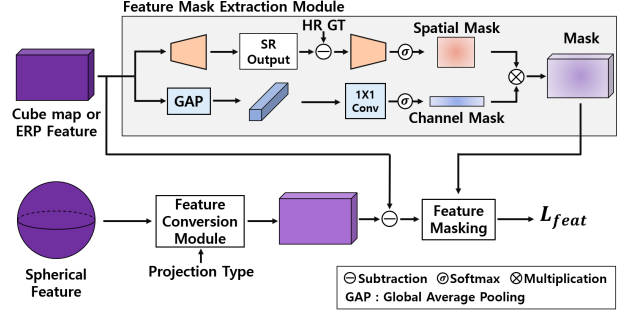


Figure 7. The proposed feature loss between the spherical and ERP features.

on the approximated rectangular sphere cell, we finally formulate the sphere-oriented cell decoding value as:

$$\begin{pmatrix} \overrightarrow{\Delta x} \\ \overrightarrow{\Delta y} \end{pmatrix} \approx \begin{pmatrix} \overrightarrow{\Delta x_{eq}} \\ \overrightarrow{\Delta y_{eq}} \end{pmatrix} = \begin{pmatrix} c_x \overrightarrow{n_1} \\ c_y \overrightarrow{n_2} \end{pmatrix} \quad (3)$$

$$\Rightarrow c = [c_x, c_y] = \left( \frac{|\overrightarrow{\Delta x_{eq}}|}{|\overrightarrow{n_1}|}, \frac{|\overrightarrow{\Delta y_{eq}}|}{|\overrightarrow{n_2}|} \right) \quad (4)$$

As a result, we can predict the RGB value  $I(X, Y)$  for any point on the projected plane based on the following equation,

$$\begin{aligned} I(X, Y) &= I(\theta, \phi, c) \\ &= \sum_{j=1}^3 \frac{A_j}{A} \cdot f_{dec}(z_j, [\gamma(r_j), \gamma(\theta_j)], [c_x, c_y]) \end{aligned} \quad (5)$$

### 3.3. Loss Function

We train the proposed framework using two loss terms. First, we use the multi-scale L1 loss. With the L1 loss defined at the multiple scales, our framework can learn more about various relative coordinates and cell decoding values. Second, we design a feature loss module to measure the similarity between the features extracted from the sphere and other projection types.

As shown in fig. 7, we design a feature mask from the ERP or cube map feature. The spatial part of the mask is generated from the difference between the predicted SR ODI and HR ground truth. The channel part of the mask is generated from the features via channel-wise global average pooling. In this way, we get the feature mask emphasizing the relevant part with high accuracy. Also, the spherical features are converted to the shapes of other projection types via the SLIIF feature conversion module. Finally, the converted features are then subtracted and masked to formulate the feature loss  $L_{feat}$ . The total loss is as follows.

$$Loss = \frac{1}{N} \sum_{j=1}^N \| I_j^{est} - I_j^{gt} \|_1 + \lambda L_{feat} \quad (6)$$

Table 1. ERP SR results on the ODI-SR and SUN 360 Panorama Dataset. **Bold** indicates the best results.

Scale	x8				x16			
	ODI-SR		SUN 360 Panorama		ODI-SR		SUN 360 Panorama	
	WS-PSNR	WS-SSIM	WS-PSNR	WS-SSIM	WS-PSNR	WS-SSIM	WS-PSNR	WS-SSIM
Bicubic	19.64	0.5908	19.72	0.5403	17.12	0.4332	17.56	0.4638
SRCNN [11]	20.08	0.6112	19.46	0.5701	18.08	0.4501	17.95	0.4684
VDSR [17]	20.61	0.6195	19.93	0.5953	18.24	0.4996	18.21	0.4867
LapSRN [18]	20.72	0.6214	20.05	0.5998	18.45	0.5161	18.46	0.5068
MemNet [38]	21.73	0.6284	21.08	0.6015	20.03	0.5411	19.88	0.5401
MSRN [21]	22.29	0.6315	21.34	0.6002	20.05	0.5416	19.87	0.5316
EDSR [22]	23.97	0.6417	22.46	0.6341	21.12	0.5698	21.06	0.5645
D-DBPN [12]	24.15	0.6573	23.70	0.6421	21.25	0.5714	21.08	0.5646
RCAN [45]	24.26	0.6628	23.88	0.6542	21.94	0.5824	21.74	0.5742
EBRN [30]	24.29	0.6656	23.89	0.6598	21.86	0.5809	21.78	0.5794
360-SS [29]	21.65	0.6417	21.48	0.6352	19.65	0.5431	19.62	0.5308
LAU-Net [10]	24.36	<b>0.6801</b>	24.02	0.6708	22.07	0.5901	21.82	0.5824
SphereSR(Ours)	<b>24.37</b>	0.6777	<b>24.17</b>	<b>0.6820</b>	<b>22.51</b>	<b>0.6370</b>	<b>21.95</b>	<b>0.6342</b>

## 4. Experiments

### 4.1. Dataset and Implementation

We train and test SphereSR using the ODI-SR dataset [10] and SUN360 panorama dataset [43]. For training, 750 out of 800 ODI-SR training images are used and the remaining 50 images are used for validation. For testing, we use 100 images from the ODI-SR test dataset and another 100 images from the SUN360 panorama dataset. The resolution of an HR ODI is  $1024 \times 2048$ , and training is performed for the scale factor  $\times 8$  and  $\times 16$ . As shown in Fig. 3, SphereSR takes an image on icosahedron as an input converted from LR ODIs, and the icosahedron subdivision levels for the scale  $\times 8$  and  $\times 16$  are set to 5 and 6, respectively. The spherical feature extractor is implemented using GA-conv based on EDSR [22] and outputs a feature with 128 dimensions. The RGB prediction decoding function  $f_{dec}$  is a 5-layer MLP, and the hidden layer dimension is 256. The EDSR model pre-trained with the ODI-SR dataset is used to extract features from ERP and cube map images for feature loss. SphereSR is trained for 500 epochs using the Adam Optimizer with batch size 1. The initial learning rate is set to 0.0001 and reduced by 10 times after 400 epochs. The feature loss scale parameter  $\lambda$  is set to 0 for the first 100 epochs and set to 0.3 for the rest of the training.

### 4.2. Evaluation on ERP

We use the ODI-SR and SUN360 Panorama datasets for evaluation. We compare SphereSR with 9 models for 2D SISR, including SRCNN [11], VDSR [17], LapSRN [18], MemNet [38], MSRN [21], EDSR [22], D-DBPN [12], RCAN [45], EBRN [30] and 2 models for ODI-SR, i.e., 360-SS [29] and LAU-Net [10]. We use WS-PSNR [47] and WS-SSIM [47] as the evaluation metrics.

**Quantitative results.** Table 1 shows the quantitative comparison for  $\times 8$  and  $\times 16$  SR on the ODI-SR and SUN 360 panorama datasets. As can be seen, SphereSR outperforms

all the compared methods on both datasets except the case of  $\times 8$  SR on the ODI-SR dataset, where SphereSR shows comparable performance with LAU-Net. However, for  $\times 16$  SR, SphereSR has the higher performance compared to LAU-Net in WS-PSNR and WS-SSIM performance on both ODI-SR and SUN360 panorama datasets.

**Qualitative comparison.** Figure 8 shows the visual comparison of the  $\times 8$  SR images on the ODI-SR dataset. As can be seen, SphereSR reconstructs clear textures and more accurate structures, while other compared methods suffer from the problems of blurred edges or distorted structures. From the visual comparison, we can conclude that SphereSR produces the texture of repeated patterns more accurately than ERP networks.

### 4.3. SR for Other Projection Types

In this section, we verify whether the proposed SphereSR, trained using the ERP images on the ODI-SR dataset, can perform well for any projection type. We first conduct an experiment on the conversion to FOV  $90^\circ$  perspective image with a size  $512 \times 512$ . We then conduct another experiment on the conversion to FOV  $180^\circ$  fisheye image with a size  $1024 \times 1024$ . In addition, we use circular fisheye projection, one of several types of fisheye projections. To compare with other SR models, we use bicubic interpolation to convert to the desired projection type. The ERP GT image is also interpolated using the bicubic method to the desired projection type for performance evaluation. We use PSNR and SSIM as the evaluation metrics. Note that we select five random directions, generate a projection output suitable for the corresponding direction, and calculate the mean value for PSNR and SSIM.

**Perspective Image.** Table 2 shows the quantitative results for perspective image SR. SphereSR again achieves the best performance on both ODI-SR and SUN360 datasets. LAU-Net [10] achieves the PSNR values of 26.39dB and 24.33dB on both datasets, respectively. By contrast, our method

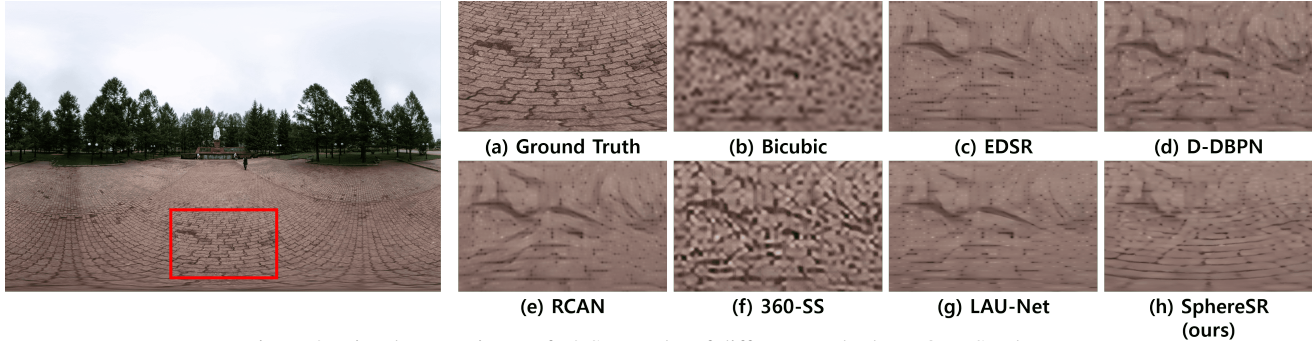


Figure 8. Visual comparisons of x8 SR results of different methods on ODI-SR dataset.

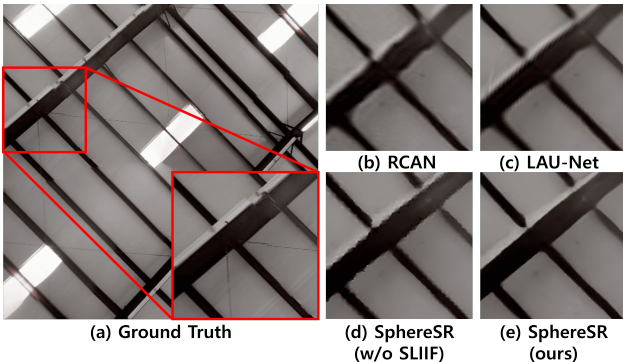


Figure 9. Visual comparison for x8 SR of perspective images on ODI-SR dataset.

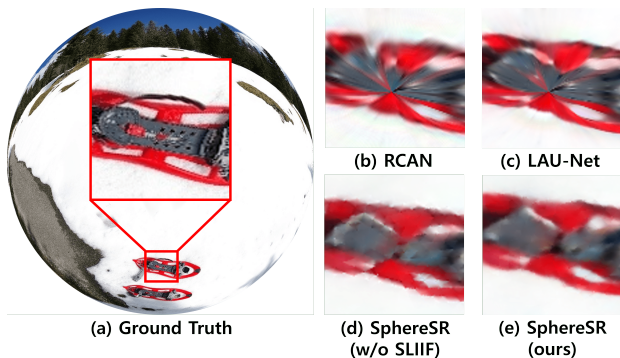


Figure 10. Visual comparison for x8 SR of fisheye images on ODI-SR dataset

significantly surpasses LAU-Net and achieves the highest PSNR values of 26.76dB and 24.46dB on both datasets, respectively. In addition, when removing the SLIIF component in SphereSR, the PSNR values drop by 0.1dB and 0.14dB, respectively. In Fig. 9, we show a visual comparison between SphereSR with SLIIF, SphereSR without SLIIF, RCAN [45] and LAU-Net [10]. As can be seen, SphereSR reconstructs clear straight lines and textures rather than other compared methods RCAN(b) and LAU-Net(c). Also, as a comparison for the usage of SLIIF(d,e), triangle-shaped artifacts are created when SLIIF is not used(d), but it can be confirmed that clear straight lines are created when SLIIF is used(e).

**Fisheye.** Table. 2 shows the quantitative results for fish-eye image SR. It can be seen that SphereSR has the highest performance regarding the PSNR and SSIM values on the ODI-SR and SUN360 panorama datasets. Among the methods for 2D SISR, RCAN achieves the second-highest PSNR value of 24.40dB on the ODI-SR dataset. On the SUN360 panorama dataset, LAU-Net achieves the second-highest PSNR of 24.97dB. Our method shows the highest PSNR and SSIM values, showing the best SR performance. In Fig. 10, we show a visual comparison between SphereSR with SLIIF, SphereSR without SLIIF, RCAN [45] and LAU-Net [10]. Specifically, we crop the area to view the SR results at the south pole. As can be seen, RCAN(b) and LAU-Net(c) generate inappropriate textures with several lines rushing to the south pole. On the other hand, SphereSR(w/o SLIIF)(d) and SphereSR(w/ SLIIF)(e) do not have such a problem. Moreover, In the case of (e), it eliminates the triangle-shaped artifact generated in (d).

#### 4.4. Ablation Study and Analysis

In this section, we study the effectiveness for each of our proposed modules, *e.g.*, GA-Conv, SLIIF, and feature loss. In addition, we validate the memory load of CNN implementation between using the data structure in our GA-Conv and the existing SpherePHD [20].

**GA-Conv.** We compare the results of Models 1 and 3 in Table 3 when adding or removing GA-Conv. GA-Conv is used in the feature extraction module to obtain the feature vector to be used in SLIIF. If GA-Conv is not used, the kernel weight sharing proposed by SpherePHD [20], which gives 180 degrees rotation per kernel, is used. Table 3 shows that using GA-Conv improves PSNR score by 0.14dB and 0.12dB in ODI-SR and SUN360 Panorama datasets, respectively, for  $\times 8$  SR.

**SLIIF.** SphereSR uses SLIIF to present SR results for the ERP projection type through feature vectors presented on the sphere. Same as the method mentioned in [32], we implement a pixel-shuffle algorithm capable of performing SR on the Icosahedron without SLIIF for performance comparison. When using the pixel-shuffle, the last feature map was subdivided by scale factor multiple, and then the fi-

Table 2. Perspective and fisheye SR results on the ODI-SR and SUN 360 Panorama Dataset. **Bold** indicates the best results.

Projection Type	Perspective				Fisheye			
	90				180			
	ODI-SR		SUN 360 Panorama		ODI-SR		SUN 360 Panorama	
Method	PSNR	SSIM	PSNR	SSIM	PSNR	SSIM	PSNR	SSIM
Bicubic	25.40	0.6858	23.49	0.6516	23.27	0.7117	22.75	0.7157
SRCNN [11](+Bicubic)	26.04	0.7005	23.98	0.6654	23.92	0.7246	23.47	0.7295
EDSR [22](+Bicubic)	26.53	0.7192	24.91	0.6916	24.21	0.7323	23.98	0.7452
D-DBPN [12](+Bicubic)	26.59	0.7139	24.63	0.6836	24.39	0.7308	24.02	0.7401
RCAN [45](+Bicubic)	26.70	0.7191	24.81	0.6901	24.40	0.7348	24.08	0.7452
360-SS [29](+Bicubic)	23.28	0.6528	21.95	0.6205	22.00	0.6957	21.61	0.6962
LAU-Net [10](+Bicubic)	26.39	0.7197	24.72	0.6943	24.33	0.7346	24.97	0.7727
SphereSR(w/o SLIIF)(+Bicubic)	26.66	0.7176	24.83	0.6930	24.32	0.7345	25.00	0.7477
SphereSR(Ours)	<b>26.76</b>	<b>0.7208</b>	<b>24.97</b>	<b>0.6962</b>	<b>24.46</b>	<b>0.7393</b>	<b>25.14</b>	<b>0.7780</b>

Table 3. Ablation studies on ERP SR on ODI-SR and SUN360 Panorama Dataset for both  $\times 8$  and  $\times 16$  SR.

Scale	Component			x8				x16			
Model	GA-Conv	SLIIF	Feature loss	ODI-SR		SUN 360 Panorama		ODI-SR		SUN 360 Panorama	
				WS-PSNR	WS-SSIM	WS-PSNR	WS-SSIM	WS-PSNR	WS-SSIM	WS-PSNR	WS-SSIM
1	x	✓	x	24.20	0.6688	23.98	0.6719	22.44	0.6341	21.92	0.6318
2	✓	x	x	24.31	0.6731	24.07	0.6749	22.47	0.6335	21.92	0.6294
3	✓	✓	x	24.34	0.6765	24.10	0.6816	22.47	0.6364	21.93	0.6336
4	✓	✓	✓	24.37	0.6777	24.17	0.6820	22.51	0.6370	21.95	0.6342

Table 4. Comparisons of activation memory between SpherePHD and our data structure. The network architectures of SpherePhD and ours have the same number of convolution layers (16) and hidden feature dimension (32).

Level	4	5	6	7
SpherePHD(MB)	660	1896	6714	26032
New Data Structure(MB)	<b>374</b>	<b>724</b>	<b>2138</b>	<b>7450</b>

nal ERP output was derived using the bicubic interpolation. As can be seen in Models 2 and 3 of Table 3, using SLIIF for continuous image presentation achieves higher performance (24.34dB vs. 24.31dB) than the pixel-shuffle method of subdivision of icosahedron for  $\times 8$  SR.

**Feature loss.** We propose a feature loss that measures the feature similarity of the crucial areas through feature masking using features generated from other projection types. To confirm the effectiveness of feature loss, we compare the SR performing when adding and removing this loss. Models 3 and 4 in Table 3 show the ablation results. Performance comparison indicates a performance improvement for all metrics in  $\times 8$  and  $\times 16$  SR.

**Data Representation Efficiency.** In Sec. 3.1, we point out that the CNN imposition method of SpherePHD is not efficient for SR. We thus propose a new data structure to tackle the problem. To see how efficiently the new data structure is, we implement a simple CNN model and then conduct an experiment comparing the activation memory. The CNN model is simply a structure in which a convolution layer is stacked, the number of convolution layers is set to 16, and the hidden feature dimension is set to 32. Table. 4 shows

the experiments from input level 4 to 7. As can be verified, the new data structure in GA-Conv has a much lower activation memory. In addition, it is found that, as the input level increased, the ratio of using new data structure memory to SpherePHD decreased. Based on the result, it can be seen that the proposed data structure is more efficient in terms of memory compared to SpherePHD. Moreover, the efficiency increases as the input resolution increases.

## 5. Conclusion

In this paper, we proposed a novel framework, called SphereSR, to generate a continuous spherical image representation from an LR  $360^\circ$  image. SphereSR predicts the RGB values at the given spherical coordinates of an HR image corresponding to an arbitrary project type. We first proposed geometry-aligned convolution to represent spherical data efficiently and then proposed SLIIF to extract RGB values from the spherical coordinates. As such, SphereSR flexibly reconstructed an HR image with an arbitrary projection type and SR scale factors. Experiments on various benchmark datasets showed that our method significantly surpasses existing methods.

**Limitation and Future Work.** We focused on finding an efficient data structure and kernel weight sharing method to extract meaningful features with the ODI input based on GA-Conv (Sec. 3.1). Future studies will therefore need to improve the network architecture using the properties of ODIs compared to perspective images, and then we can achieve better SR results via SLIIF.



## References

- [1] Ivan Anokhin, Kirill Demochkin, Taras Khakhulin, Gleb Sterkin, Victor Lempitsky, and Denis Korzhenkov. Image generators with conditionally-independent pixel synthesis. In *The IEEE/CVF Conference on Computer Vision and Pattern Recognition (CVPR)*, 2021. [2](#)
- [2] Zafer Arican and Pascal Frossard. L1 regularized super-resolution from unregistered omnidirectional images. pages 829–832, 2009. [2](#)
- [3] Zafer Arican and Pascal Frossard. Joint registration and super-resolution with omnidirectional images. *IEEE Transactions on Image Processing*, 20(11):3151–3162, 2011. [1](#)
- [4] Zafer Arican and Pascal Frossard. Joint registration and super-resolution with omnidirectional images. volume 20, pages 3151–3162, 2011. [2](#)
- [5] Luigi Bagnato, Yannick Boursier, Pascal Frossard, and Pierre Vanderghyest. Plenoptic based super-resolution for omnidirectional image sequences. In *2010 IEEE International Conference on Image Processing*, pages 2829–2832. IEEE, 2010. [1](#)
- [6] Luigi Bagnato, Yannick Boursier, Pascal Frossard, and Pierre Vanderghyest. Plenoptic based super-resolution for omnidirectional image sequences. pages 2829–2832, 2010. [2](#)
- [7] Yinbo Chen, Sifei Liu, and Xiaolong Wang. Learning continuous image representation with local implicit image function. In *Proceedings of the IEEE/CVF Conference on Computer Vision and Pattern Recognition*, pages 8628–8638, 2021. [2](#), [4](#), [5](#)
- [8] T.S. Cohen, M. Geiger, J. Khler, and M. Welling. Spherical cnns. In *International Conference on Learning Representations*, pages 4302–4311, 2018. [2](#)
- [9] Benjamin Coors, Alexandru Paul Condurache, and Andreas Geiger. Spherenet: Learning spherical representations for detection and classification in omnidirectional images. In *Proceedings of the European Conference on Computer Vision (ECCV)*, pages 518–533, 2018. [3](#)
- [10] Xin Deng, Hao Wang, Mai Xu, Yichen Guo, Yuhang Song, and Li Yang. Lau-net: Latitude adaptive upscaling network for omnidirectional image super-resolution. In *Proceedings of the IEEE/CVF Conference on Computer Vision and Pattern Recognition*, pages 9189–9198, 2021. [1](#), [2](#), [6](#), [7](#), [8](#)
- [11] Chao Dong, Chen Change Loy, Kaiming He, and Xiaoou Tang. Image super-resolution using deep convolutional networks. In *IEEE Transactions on Pattern Analysis and Machine Intelligence*, volume 38, pages 295–307, 2016. [6](#), [8](#)
- [12] Muhammad Haris, Greg Shakhnarovich, and Norimichi Ukita. Deep back-projection networks for super-resolution. In *IEEE Conference on Computer Vision and Pattern Recognition (CVPR)*, 2018. [6](#), [8](#)
- [13] Xuecai Hu, Haoyuan Mu, Xiangyu Zhang, Zilei Wang, Tieniu Tan, and Jian Sun. Meta-sr: A magnification-arbitrary network for super-resolution. In *IEEE Conference on Computer Vision and Pattern Recognition*, 2019. [2](#)
- [14] Phillip Isola, Jun-Yan Zhu, Tinghui Zhou, and Alexei A Efros. Image-to-image translation with conditional adversarial networks. In *Proceedings of the IEEE conference on computer vision and pattern recognition*, pages 1125–1134, 2017. [2](#)
- [15] Hiroshi Kawasaki, Katsushi Ikeuchi, and Masao Sakauchi. Super-resolution omnidirectional camera images using spatio-temporal analysis. volume 89, pages 47–59, 2006. [2](#)
- [16] Hee-Jae Kim, Je-Won Kang, and Byung-Uk Lee. Super-resolution of multi-view erp 360-degree images with two-stage disparity refinement. In *2020 Asia-Pacific Signal and Information Processing Association Annual Summit and Conference (APSIPA ASC)*, pages 1283–1286. IEEE, 2020. [1](#)
- [17] Jiwon Kim, Jung Kwon Lee, and Kyoung Mu Lee. Accurate image super-resolution using very deep convolutional networks. In *2016 IEEE Conference on Computer Vision and Pattern Recognition (CVPR)*, pages 1646–1654, 2016. [6](#)
- [18] Wei-Sheng Lai, Jia-Bin Huang, Narendra Ahuja, and Ming-Hsuan Yang. Deep laplacian pyramid networks for fast and accurate super-resolution. In *2017 IEEE Conference on Computer Vision and Pattern Recognition (CVPR)*, pages 5835–5843, 2017. [1](#), [6](#)
- [19] Christian Ledig, Lucas Theis, Ferenc Huszár, Jose Caballero, Andrew Cunningham, Alejandro Acosta, Andrew Aitken, Alykhan Tejani, Johannes Totz, Zehan Wang, et al. Photo-realistic single image super-resolution using a generative adversarial network. In *Proceedings of the IEEE conference on computer vision and pattern recognition*, pages 4681–4690, 2017. [1](#)
- [20] Yeonkun Lee, Jaeseok Jeong, Jongseob Yun, Wonjune Cho, and Kuk-Jin Yoon. Spherephd: Applying cnns on 360° images with non-euclidean spherical polyhedron representation. In *IEEE Transactions on Pattern Analysis and Machine Intelligence*, 2020. [3](#), [4](#), [7](#)
- [21] Juncheng Li, Faming Fang, Kangfu Mei, and Guixu Zhang. Multi-scale residual network for image super-resolution. In *ECCV*, 2018. [6](#)
- [22] Bee Lim, Sanghyun Son, Heewon Kim, Seungjun Nah, and Kyoung Mu Lee. Enhanced deep residual networks for single image super-resolution. In *Proceedings of the IEEE conference on computer vision and pattern recognition workshops*, pages 136–144, 2017. [1](#), [2](#), [6](#), [8](#)
- [23] Hongying Liu, Zubo Ruan, Chaowei Fang, Peng Zhao, Fanhua Shang, Yuan yuan Liu, and Lijun Wang. A single frame and multi-frame joint network for 360-degree panorama video super-resolution. In *ArXiv*, 2020. [2](#)
- [24] Lars M. Mescheder, Michael Oechsle, Michael Niemeyer, Sebastian Nowozin, and Andreas Geiger. Occupancy networks: Learning 3d reconstruction in function space. *IEEE/CVF Conference on Computer Vision and Pattern Recognition (CVPR)*, pages 4455–4465, 2019. [2](#)
- [25] Ben Mildenhall, Pratul P. Srinivasan, Matthew Tancik, Jonathan T. Barron, Ravi Ramamoorthi, and Ren Ng. Nerf: Representing scenes as neural radiance fields for view synthesis. In *European Conference on Computer Vision*, 2020. [2](#), [4](#)
- [26] Hajime Nagahara, Yasushi Yagi, and Masahiko Yachida. Super-resolution from an omnidirectional image sequence. In *2000 26th Annual Conference of the IEEE Industrial Electronics Society. IECON 2000. 2000 IEEE International Conference on Industrial Electronics, Control and Instrumentation. 21st Century Technologies*, volume 4, pages 2559–2564. IEEE, 2000. [1](#)

- [27] Hajime Nagahara, Yasusi Yagi, and Masahiko Yachida. Super-resolution from an omnidirectional image sequence. In *2000 26th Annual Conference of the IEEE Industrial Electronics Society. IECON 2000. 2000 IEEE International Conference on Industrial Electronics, Control and Instrumentation. 21st Century Technologies*, volume 4, pages 2559–2564 vol.4, 2000. 2
- [28] Akito Nishiyama, Satoshi Ikehata, and Kiyoharu Aizawa. 360° single image super resolution via distortion-aware network and distorted perspective images. In *ICIP 2021*, 2021. 2
- [29] Cagri Ozcinar, Aakanksha Rana, and Aljosa Smolic. Super-resolution of omnidirectional images using adversarial learning. In *2019 IEEE 21st International Workshop on Multimedia Signal Processing (MMSP)*, pages 1–6. IEEE, 2019. 1, 2, 6, 8
- [30] Yajun Qiu, Ruxin Wang, Dapeng Tao, and Jun Cheng. Embedded block residual network: A recursive restoration model for single-image super-resolution. In *2019 IEEE/CVF International Conference on Computer Vision (ICCV)*, pages 4179–4188, 2019. 6
- [31] Vida Fakour Sevom, Esin Guldogan, and J. Kämäräinen. 360 panorama super-resolution using deep convolutional networks. In *VISIGRAPP*, 2018. 2
- [32] Wenzhe Shi, Jose Caballero, Ferenc Huszar, Johannes Totz, Andrew P. Aitken, Rob Bishop, Daniel Rueckert, and Zehan Wang. Real-time single image and video super-resolution using an efficient sub-pixel convolutional neural network. In *Proceedings of the IEEE Conference on Computer Vision and Pattern Recognition (CVPR)*, June 2016. 7
- [33] Vincent Sitzmann, Michael Zollhöfer, and Gordon Wetzstein. Scene representation networks: Continuous 3d-structure-aware neural scene representations. In *Advances in Neural Information Processing Systems*, 2019. 2
- [34] Ivan Skorokhodov, Savva Ignatyev, and Mohamed Elhoseiny. Adversarial generation of continuous images. In *The IEEE/CVF Conference on Computer Vision and Pattern Recognition (CVPR)*, 2021. 2
- [35] Sanghyun Son and Kyoung Mu Lee. SRWarp: Generalized image super-resolution under arbitrary transformation. In *CVPR*, 2021. 2
- [36] Yu-Chuan Su and Kristen Grauman. Kernel transformer networks for compact spherical convolution. In *IEEE/CVF Conference on Computer Vision and Pattern Recognition*, pages 9434–9443, 2019. 3
- [37] Yule Sun, Ang Lu, and Lu Yu. Weighted-to-spherically-uniform quality evaluation for omnidirectional video. In *IEEE Signal Processing Letters*, volume 24, pages 1408–1412, 2017. 1, 2
- [38] Ying Tai, Jian Yang, Xiaoming Liu, and Chunyan Xu. Memnet: A persistent memory network for image restoration. In *2017 IEEE International Conference on Computer Vision (ICCV)*, pages 4549–4557, 2017. 1, 6
- [39] Matthew Tancik, Pratul P. Srinivasan, Ben Mildenhall, Sara Fridovich-Keil, Nithin Raghavan, Utkarsh Singhal, Ravi Ramamoorthi, Jonathan T. Barron, and Ren Ng. Fourier features let networks learn high frequency functions in low dimensional domains. In *In Advances in Neural Information Processing Systems (NeurIPS)*, volume abs/2006.10739, 2020. 4
- [40] Longguang Wang, Yingqian Wang, Zaiping Lin, Jungang Yang, Wei An, and Yulan Guo. Learning a single network for scale-arbitrary super-resolution. In *IEEE/CVF International Conference on Computer Vision*, 2021. 2
- [41] Lin Wang and Kuk-Jin Yoon. Semi-supervised student-teacher learning for single image super-resolution. *Pattern Recognition*, 121:108206, 2022. 1
- [42] Xintao Wang, Ke Yu, Shixiang Wu, Jinjin Gu, Yihao Liu, Chao Dong, Yu Qiao, and Chen Change Loy. Esrgan: Enhanced super-resolution generative adversarial networks. In *Proceedings of the European conference on computer vision (ECCV) workshops*, pages 0–0, 2018. 1
- [43] Jianxiong Xiao, Krista A Ehinger, Aude Oliva, and Antonio Torralba. Recognizing scene viewpoint using panoramic place representation. In *2012 IEEE Conference on Computer Vision and Pattern Recognition*, pages 2695–2702. IEEE, 2012. 6
- [44] Chao Zhang, Stephan Liwicki, William Smith, and Roberto Cipolla. Orientation-aware semantic segmentation on icosahedron spheres. *IEEE/CVF International Conference on Computer Vision*, pages 3532–3540, 2019. 3
- [45] Yulun Zhang, Kunpeng Li, Kai Li, WangLichen, Bineng Zhong, and Yun Raymond Fu. Image super-resolution using very deep residual channel attention networks. In *ECCV*, 2018. 1, 6, 7, 8
- [46] Yupeng Zhang, Hengzhi Zhang, Daojing Li, Li-Yan Liu, Hong Yi, Wei Wang, Hiroshi Suitoh, and Makoto Odamaki. Toward real-world panoramic image enhancement. *2020 IEEE/CVF Conference on Computer Vision and Pattern Recognition Workshops (CVPRW)*, pages 2675–2684, 2020. 2
- [47] Yufeng Zhou, Mei Yu, Hualin Ma, Hua Shao, and Gangyi Jiang. Weighted-to-spherically-uniform ssim objective quality evaluation for panoramic video. In *2018 14th IEEE International Conference on Signal Processing (ICSP)*, pages 54–57, 2018. 1, 2, 6

# SphereSR: 360° Image Super-Resolution with Arbitrary Projection via Continuous Spherical Image Representation

## –Supplementary Material–

Youngho Yoon, Inchul Chung, Lin Wang, and Kuk-Jin Yoon  
 Visual Intelligence Lab., KAIST, Korea

{dudgh1732, inchul1221, wanglin, kjyoon}@kaist.ac.kr

### Abstract

Due to the lack of space in the main paper, we provide more details of the proposed methods and experimental results in the supplementary material. Specifically, in Sec.1, we provide more details of the feature extraction module for spherical images. Sec.2 explains explicitly the proposed sphere-oriented cell decoding in SLIIF module. Lastly, Sec.3 presents additional results about experiments and ablation study.

## 1. More Details of Feature Extraction for Spherical Images

### 1.1. Data structure

As shown in Fig. 1, we make the implementation of up/downward kernel possible with  $5 \times 3$  convolution by using the proposed new data structure. At this time, among the pixels of the  $5 \times 3$  convolution kernel, 5 pixels not included in the actual kernel are always multiplied by weight 0, and the weight update is not performed.

We also always do feature padding with neighborhood pixels right before convolution to avoid losing the continuity of the spherical data structure. The padding size is  $2 \times 1$  padding considering the kernel size.

Finally, as the convolutional kernels for odd-numbered and even-numbered rows are different, the convolution stride for the row axis is set to 2 such that convolution for the kernel can be performed for each row. After convolution for each kernel, two feature maps are concatenated according to the order of rows.

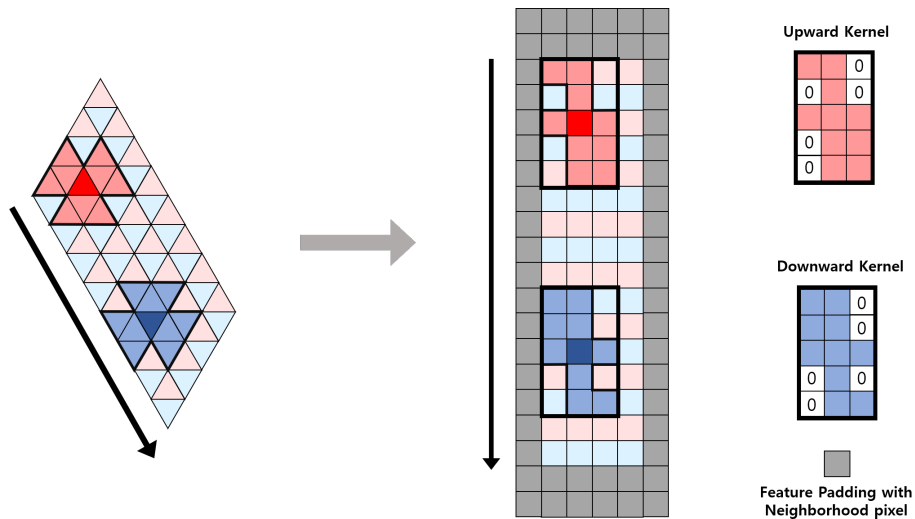


Figure 1. Proposed new data structure.

## 1.2. Kernel Weight Sharing

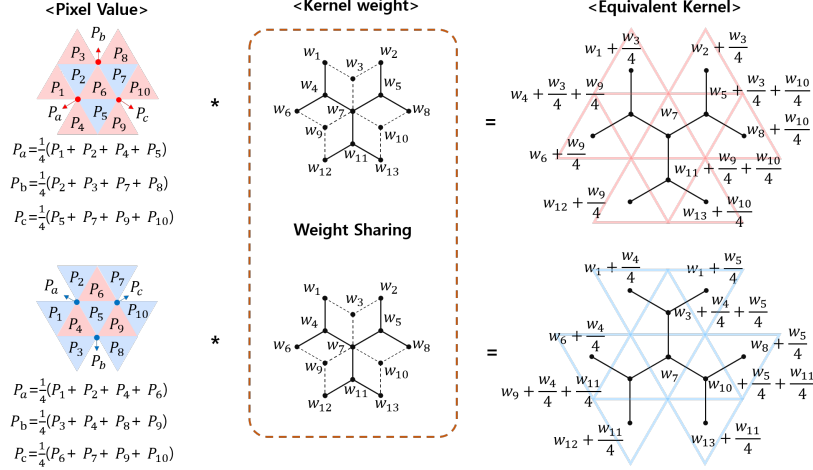


Figure 2. Geometry-Aligned Convolution(GA-Conv) and equivalent kernel.

In this subsection, we describe in detail the derivation of the kernel weight sharing scheme for GA-Conv (Geometry-Aligned Convolution). As shown in Fig. 2, we set the three vertices of the center pixel to the imaginary pixels  $P_a, P_b, P_c$  to make the shape of the pixel combination the same. At this time, each pixel can be regarded as the midpoint of the surrounding four pixels. Therefore, the values of pixels  $P_a, P_b, P_c$  are set as the mean value of four pixels through the formulas in the Fig. 2. We present a way to utilize weight sharing without actually creating a pixel when implementing this setting. As can be seen from Fig. 2, the convolution with pixel values and kernel weights is the same as the value convolutional using the equivalent kernel. Therefore, an appropriate weight sharing scheme is used to use GA-Conv, and through this, more sophisticated kernel weight sharing is possible without kernel rotation previously performed in SpherePHD.

## 2. Sphere-oriented Cell Decoding

In this section, we explain more details about sphere-oriented cell-decoding method. A rectangle  $\overrightarrow{\Delta X}, \overrightarrow{\Delta Y}$  on the projected plane makes parallelogram  $\overrightarrow{\Delta x}, \overrightarrow{\Delta y}$  on the unit sphere. To define a cell decoding according to point  $p$  on unit sphere, we initially define a vector  $(\vec{n}_1, \vec{n}_2)$ . Let  $o = \text{center point}(r = 0)$ ,  $p = (\theta, \phi)$  s.t. point  $p$  we want to get RGB and  $v_x = (\theta_v, \phi_v)$  s.t. one of vertices 1, 2, 3. Then,

$$\vec{n}_1 = \overrightarrow{v_x p} = (\theta - \theta_v)\hat{\theta} + (\phi - \phi_v)\sin\theta\hat{\phi} \quad (1)$$

$$\vec{n}_2 = \overrightarrow{op} \times \vec{n}_1 = -(\phi - \phi_v)\sin\theta\hat{\theta} + (\theta - \theta_v)\hat{\phi} \quad (2)$$

To make  $(\vec{n}_1, \vec{n}_2)$  as unit vectors, the vectors are scaled as  $\vec{n}_1 \leftarrow \vec{n}_1 / \|\vec{n}_1\|$  and  $\vec{n}_2 \leftarrow \vec{n}_2 / \|\vec{n}_2\|$ . By these equations, we can find the variables  $\alpha_1, \beta_1, \alpha_2, \beta_2$  that satisfies the following equation,

$$\begin{pmatrix} \hat{\theta} \\ \hat{\phi} \end{pmatrix} = \begin{pmatrix} \alpha_1 & \beta_1 \\ \alpha_2 & \beta_2 \end{pmatrix} \begin{pmatrix} \vec{n}_1 \\ \vec{n}_2 \end{pmatrix} \quad (3)$$

To denote vectors  $\overrightarrow{\Delta x}, \overrightarrow{\Delta y}$  representing parallelogram sphere cells using  $\vec{n}_1, \vec{n}_2$ , we first denote using  $\hat{\theta}, \hat{\phi}$  through the projection process of each projection type, as shown in Fig. 3. Therefore, we have to find as the equation,

$$\begin{pmatrix} \overrightarrow{\Delta x} \\ \overrightarrow{\Delta y} \end{pmatrix} = \begin{pmatrix} \gamma_1\hat{\theta} + \delta_1\hat{\phi} \\ \gamma_2\hat{\theta} + \delta_2\hat{\phi} \end{pmatrix} \Rightarrow \begin{matrix} \text{decided by output of} \\ \text{projection type} \end{matrix} \quad (4)$$

Let  $P$  be the point  $(X, Y)$  where point  $p$  is projected onto the projected plane. As the derivation results, each projection can be organized as a table. 1. Fisheye projection type is the result of the projection process by setting the reflective surface  $Z = F(X, Y)$  as mentioned in [?]. Also, in case of Perspective projection,

$$\alpha = \frac{1}{\sqrt{\tan^2\phi + \frac{1}{\tan^2\theta \cos^2\phi}}}, \Delta X = \frac{2 \tan \frac{M}{2}}{b}, \Delta Y = \frac{2 \tan \frac{N}{2}}{a} \quad (5)$$

Table 1. Derivation of  $\vec{\Delta x}, \vec{\Delta y}$  for various projection types.

ERP	Perspective
$\begin{pmatrix} \vec{\Delta x} \\ \vec{\Delta y} \end{pmatrix} = \begin{pmatrix} \Delta Y \sin \theta & 0 \\ 0 & \Delta X \end{pmatrix} \begin{pmatrix} \hat{\theta} \\ \hat{\phi} \end{pmatrix}$	$\begin{pmatrix} \vec{\Delta x} \\ \vec{\Delta y} \end{pmatrix} = \begin{pmatrix} \alpha \Delta X \cos \theta \sin \phi & \alpha \Delta X \cos \phi \\ -\alpha \Delta Y \sin \theta & 0 \end{pmatrix} \begin{pmatrix} \hat{\theta} \\ \hat{\phi} \end{pmatrix}$
Fisheye	
$\begin{pmatrix} \vec{\Delta x} \\ \vec{\Delta y} \end{pmatrix} = \begin{pmatrix} \alpha \Delta X \cos \theta \sin \phi + \alpha \Delta X F_X(X, Y) \cos \theta \cos \phi & \alpha \Delta X \cos \phi - \alpha \Delta X F_X(X, Y) \sin \phi \\ -\alpha \Delta Y \sin \theta + \alpha \Delta Y F_Y(X, Y) \cos \theta \cos \phi & -\alpha \Delta Y F_Y(X, Y) \sin \phi \end{pmatrix} \begin{pmatrix} \hat{\theta} \\ \hat{\phi} \end{pmatrix}$	

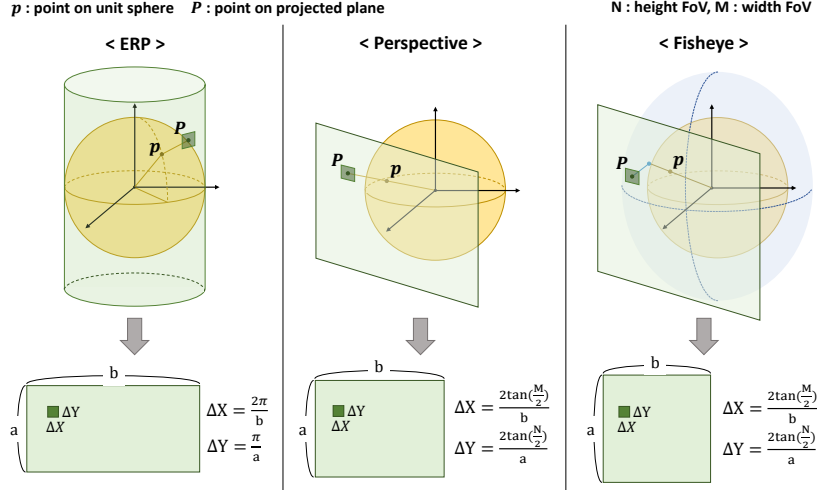


Figure 3. Visualization of projection process of each projection type.

in case of Fisheye projection,

$$\alpha = \frac{1}{\sqrt{X^2 + Y^2 + F_X(X, Y)^2}}, \Delta X = \frac{F(X', 0)}{b} \text{ s.t. } \frac{X'}{F(X', 0)} = \tan \frac{M}{2}, \Delta Y = \frac{F(0, Y')}{a} \text{ s.t. } \frac{Y'}{F(0, Y')} = \tan \frac{N}{2} \quad (6)$$

Finally, we are able to represent  $\vec{\Delta x}, \vec{\Delta y}$  using two vectors  $\vec{n}_1, \vec{n}_2$  by Eqs. (3) and (4).

$$\begin{pmatrix} \vec{\Delta x} \\ \vec{\Delta y} \end{pmatrix} = \begin{pmatrix} \gamma_1 & \delta_1 \\ \gamma_2 & \delta_2 \end{pmatrix} \begin{pmatrix} \alpha_1 & \beta_1 \\ \alpha_2 & \beta_2 \end{pmatrix} \begin{pmatrix} \vec{n}_1 \\ \vec{n}_2 \end{pmatrix} \quad (7)$$

We then find a  $\vec{\Delta x}_{eq}, \vec{\Delta y}_{eq}$  as mentioned in the main paper.

### 3. Visualization

#### 3.1. Additional Qualitative Comparison.

We additionally visualize the qualitative comparison with Ours and other methods on ODI-SR dataset and SUN360 Panorama dataset in Fig. 4 and Fig. 5. We compare the results with various projection types, ERP, perspective and fish-eye.

#### 3.2. Visualization of SR with Arbitrary Projection Types.

We additionally visualize the SR results for arbitrary projection type from LR ERP images in Fig. 6 and Fig. 7. We also visualize images for different directions to show that our model can predict SR results for arbitrary directions.

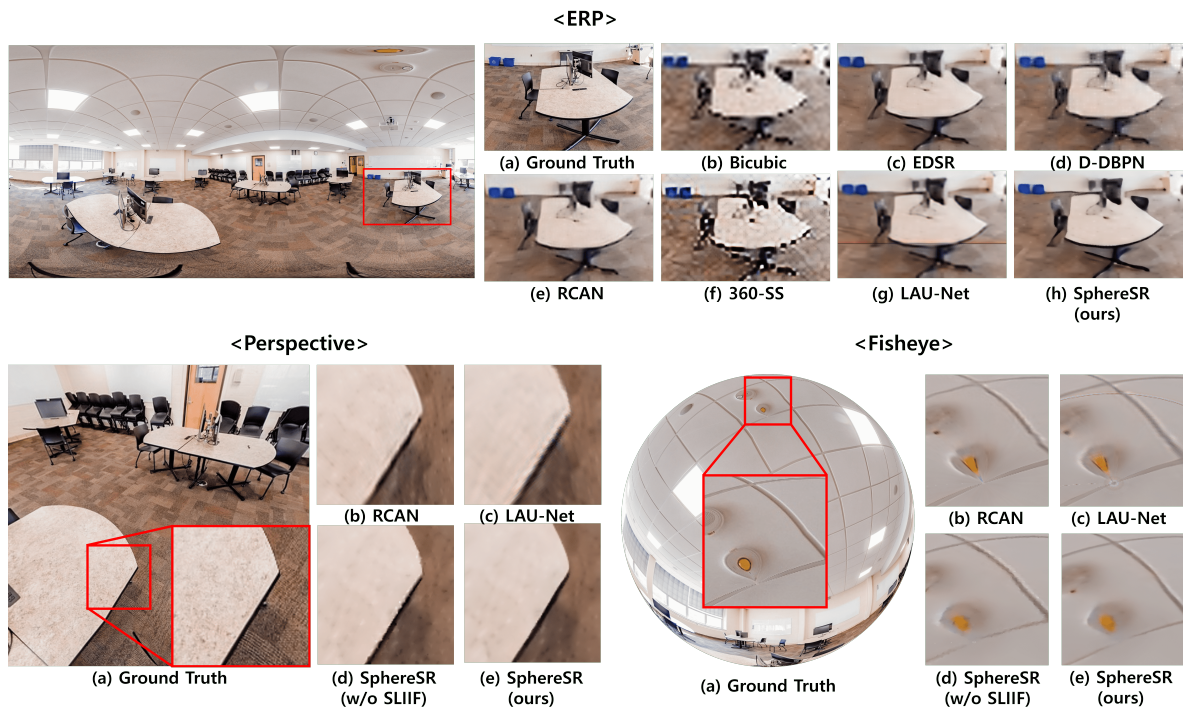


Figure 4. Visual comparisons of  $\times 8$  SR results of ERP, perspective, fisheye projection on SUN 360 Panorama dataset.

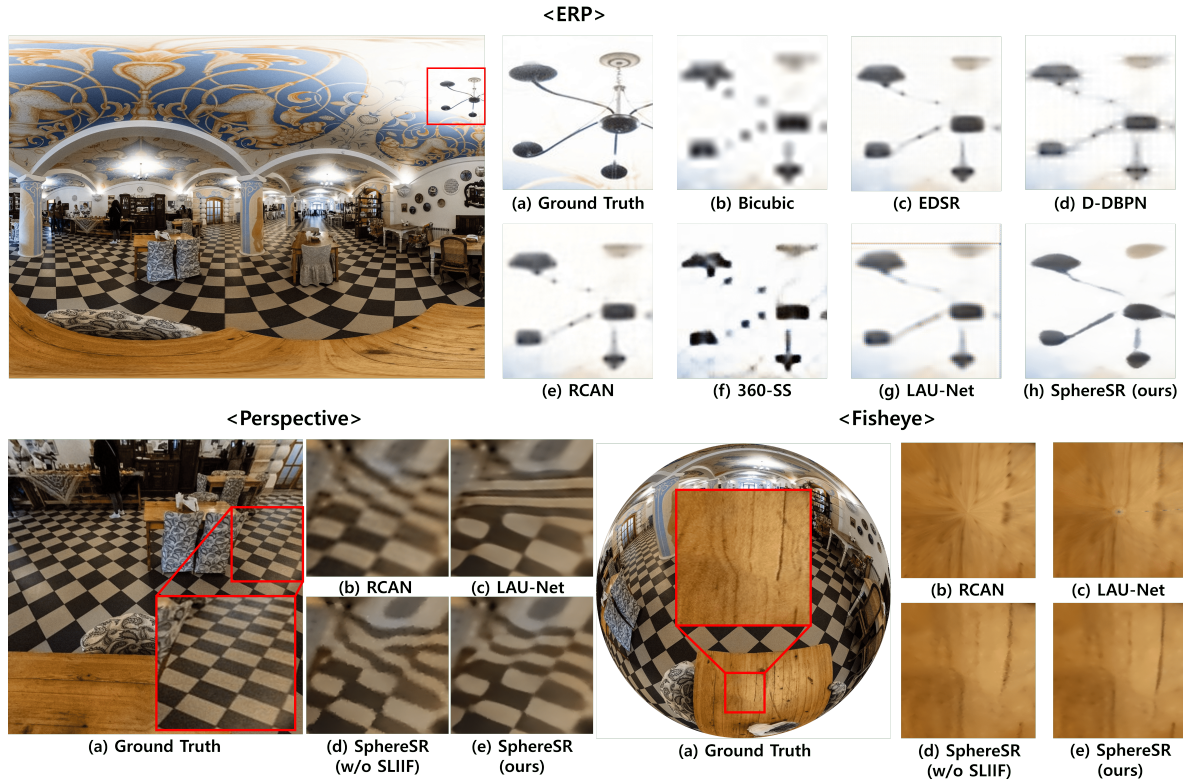


Figure 5. Visual comparisons of  $\times 8$  SR results of ERP, perspective, fisheye projection on ODI-SR dataset.



Figure 6. Visualization of  $\times 8$  SR results with various projection types on SUN360 Panorama dataset.

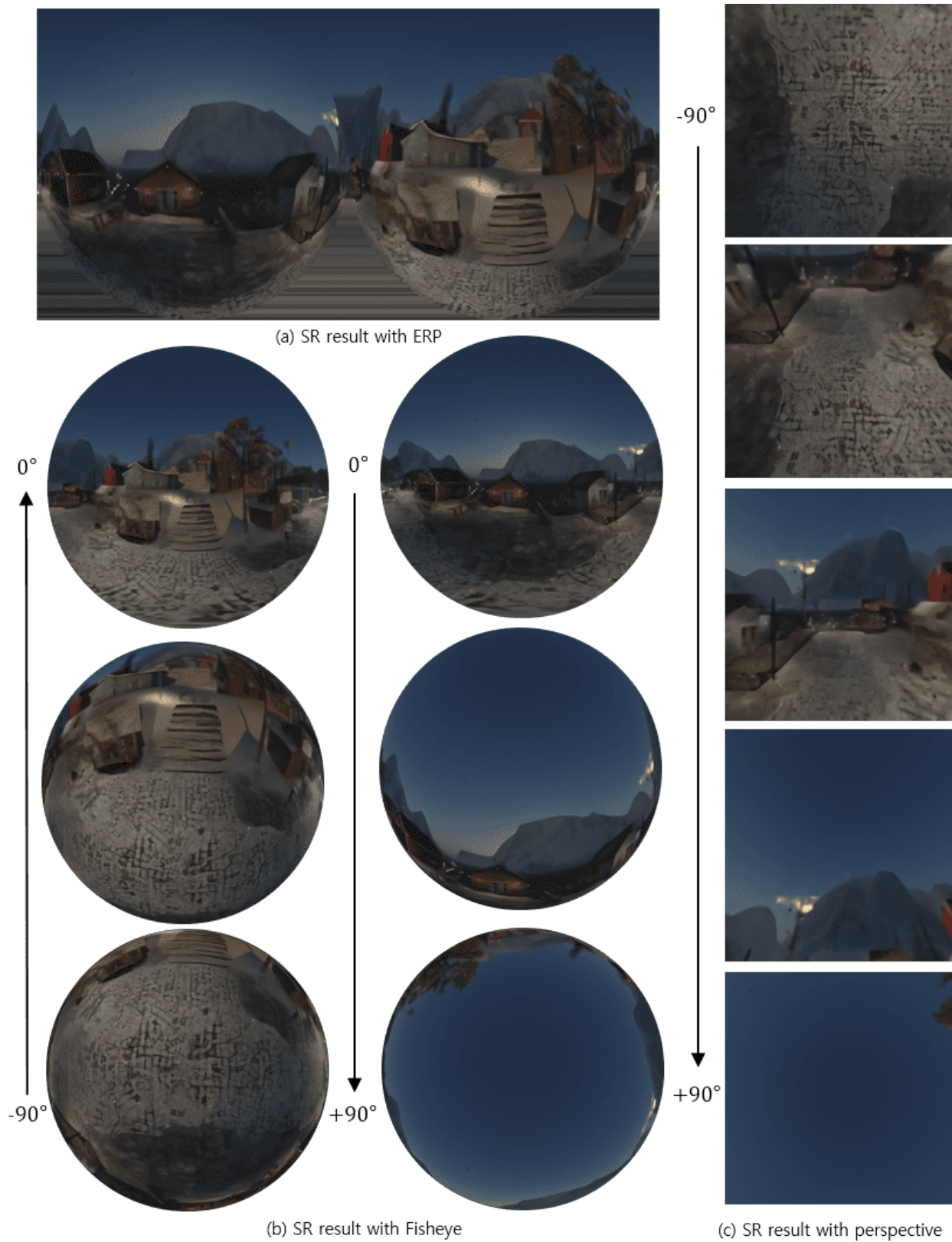


Figure 7. Visualization of  $\times 8$  SR results with various projection types on ODI-SR dataset.